Solid Freeform Fabrication 2022: Proceedings of the 33rd Annual International Solid Freeform Fabrication Symposium – An Additive Manufacturing Conference
Reviewed Paper

EFFECT OF THERMAL AGING IN THE FATIGUE LIFE OF HOT ISOSTATIC PRESSED AlSi10Mg FABRICATED BY LASER POWDER BED FUSION

S. T. Nabil[a,b], E. Arrieta[a,b], R.B. Wicker[a,b], M. Benedict[c] and F. Medina[a,b]

[a] W.M. Keck Center for 3D Innovation, The University of Texas at El Paso, TX, 79968, USA;
[b] Aerospace and Mechanical Engineering, The University of Texas at El Paso, El Paso, TX 79968, USA;
[c] Air Force Research Laboratory, Wright-Patterson Air Force Base, Dayton, OH, 45433, USA;

* Corresponding author (snabil@miners.utep.edu) at The University of Texas at El Paso

ABSTRACT

AlSi10Mg is a widely used material in the aerospace industry. Extended exposure to elevated temperatures can have a detrimental effect on it. In this work, multiple AlSi10Mg horizontal bars and vertical rods were fabricated using an L-PBF system. Following ASTM F3318-18, the material blanks were HIPed (Hot Isostatic Pressed). Emulating service temperatures, these blanks were aged at 177°C for 10, 100, and 1000h. Fatigue test specimens were machined down from the aged blanks. The machined specimens were subjected to a force-controlled fatigue test as per ASTM E466-15 with two stress levels: one within the elastic range (62MPa) of the material and another close to UTS (124MPa). The results indicated that even aging for 10h can dramatically reduce the fatigue life of the alloy. The work concludes with discussion on the reduction of fatigue life and visible progressive change in the ductility of the alloy with respect to the aging time.

Keywords
Laser Powder Bed Fusion(L-PBF), Fatigue Life, Thermal Aging, AlSi10Mg, Hot-Isostatic Pressing

Nomenclature

L-PBF – Laser Powder Bed Fusion
HIPed – Hot Isostatic Pressed
YS – Yield Strength
UTS – Ultimate Strength
HT – Heat Treatment
°C – Degree Celsius
µm – Micrometer
MPa- Megapascal
Φ – Diameter
HV- Hardness Value

INTRODUCTION

Lightweight materials are always a primary focus in the modern aerospace industry. With the expansion of additive manufacturing technology, the possibility for the fabrication of complex and lightest weight structures has surpassed from rapid prototyping and moving forward to mass production[1], [2]. 3D printing with powders has recently drawn the attention of engineers and scientists because of its versatile application in harsh environments[3]–[5]. Especially in the metal additive manufacturing sector- technologies like Powder Bed Fusion (PBF), Direct Energy Deposition (DED), Binder Jetting, etc., have constantly been used to develop complex geometries to aid modern aerospace and defense applications [6]–[9]. Thanks to improved powder materials and modern additive technologies, it is possible to manufacture lighter and cost-efficient components for the defense and aerospace sector.

High-strength aluminum alloys- Due to their low weight, superior strength, and corrosive resistance properties, are widely used materials in the industry[11]. Especially AlSi10Mg, which has a density of ~2.66g/cm^3 and a low melting point ranging from 570-590°C, is widely used to fabricate machined parts, heat exchangers, timing gears, automotive parts, and modern aerospace components[12], [13]. But, Al-Si parts are prone to porosities and defects, limiting the ability to obtain desired mechanical properties[14]–[19]. Nevertheless, it is possible to overcome such limitations by implementing powder bed fusion technology, especially Laser Powder Bed Fusion (L-PBF).

Previous studies done with AlSi10Mg alloy with L-PBF have shown that it is possible to produce parts having nominal yield stress (YS) around 300MPa in contrast to almost 170 MPa seen for casted parts[20]. In addition, Numerous investigations of the post-heat treatment (HT) process of LPBF fabricated AlSi10Mg alloy, including stress relief (SR) anneals ranging around 200-540°C for 1 to 2 hours, solution treatments up to 550°C for 2 hours, Hot Isostatic Pressing (HIP) in 100MPa nitrogen environment at temperature up to 525°C for 2hours, and tempering or aging up to 530°C at holding times up to 10 hours along with various combinations were conducted. These HT processes have resulted in a variety of mechanical properties in processed and post-processed L-PBF samples. Without HT, YS value was observed near 300MPa, and UTS value close to 480MPa while elongation was around 5 to 8%. After the HT, the YS transformed in a range of 80MPa to 170MPa with UTS in a range between 100MPa to 190MPa while varying the elongations ranging around 6 to 24%[21]–[31].

This present study is aimed to investigate the fatigue performance of thermally aged AlSi10Mg alloy samples. These blanks were fabricated using LPBF and subsequently HIPed following ASTM F3318-18 at 510°C - 520°C, 100MPa for 3 hours. Then the HIPed blanks were thermally aged at 177°C for 0,10,100 and 1000 hours in the air. Later, the specimens were machined for the fatigue test: one in the range of YS at 62MPa and another near UTS at 124MPa, and the fatigue endurance was evaluated.

METHODOLOGY

Powder Feed

AM 103C grade AlSi10Mg pre-alloyed powder (Inert gas atomized) from Valimet (Stockton, California) was used for the L-PBF system. The size and shape of the powder were analyzed using a Retsch Camsizer X2 (Haan, Germany) and shown in Figure 1. The size distribution ranged from 25 to 70 µm illustrated in where d10: 25.2µm, d50: 39µm, and d90: 59.2µm, respectively. Metallographic assessment of the internal section exhibited a micro-dendritic alpha-Al composition with secondary arm spacing of almost 1 micron, as shown in Figure 2.

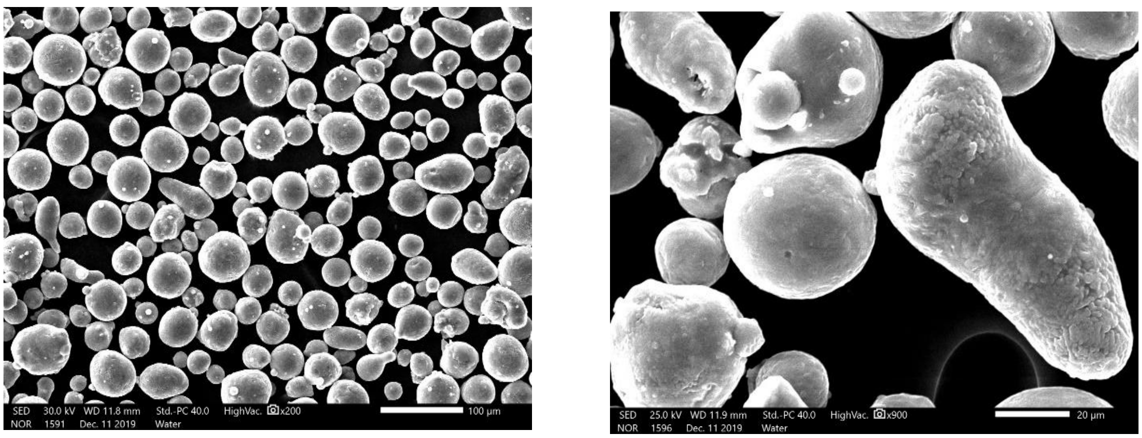

(a) (b)

Figure 1: SEM images of Gas Atomized AlSi10Mg powder a) 100µm , b) 20µm

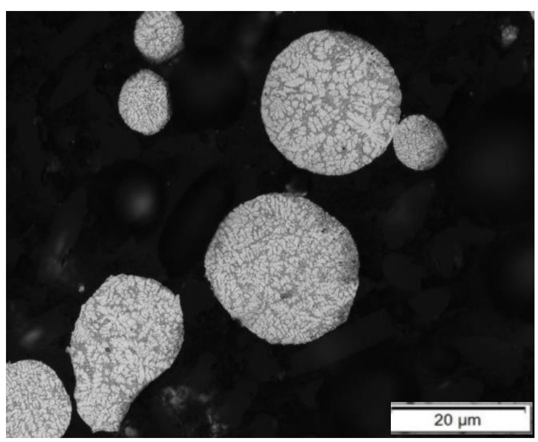

Figure 2: Section View of Powder particle revealing micro dendritic structures

EOS M290 L-PBF systems

The LPBF system used was EOS M290 (Kralling, Germany). It uses a 400W Yb-fiber laser and has an internal build volume of 250 x 250 x 325 mm[32]. A total of 48 (24 specimens in each orientation) Z-oriented vertical rods of 14mm x80 mm (Φ x H) and 24 XY-oriented bar blanks of 14 mm x 17mm x 76mm (L x W x H) were printed as test specimens.

Print Parameters

Process parameters used for the LPBF system were pre-developed (as shown in Table 1) and able to produce builds with an average density of 2.65g/cm^3. This density was determined using a gas pycnometer which is equivalent to 99.25% of the density of 2.67g/cm^3 EOS datasheet for AlSi10Mg printed in layers of 30µm with M290 systems[33].

Table 1: Process Parameters used in EOS M290

Laser Power	300W
Preheat Temperature of Bedplate	80°C
Scanning Speed	1000 mm/s
Hatch Distance	130 µm
Layer Thickness	30 µm
Print Pattern	Striped with 7mm width and 20µm overlap distance

Thermal Post-Processing: HIP and Aging

The As-build AlSi10Mg blanks and rods (a total of 48 specimens) were subjected to HIP as per ASTM F3318-18 standard[34].HIP was done at 515°C at 100MPa for 3 hours and cooled under an inert atmosphere to below 94°C. Followed by HIP, the blanks and rods were separated into four groups of twelve specimens: 6-Vertical (Z) and 6-Horizontal (XY), to be aged at 177°C for 0h, 10h, 100h, and 1000h.

Fatigue Test

The specimens were machined from aged blanks for the fatigue endurance test following as per ASTM E466-15[35]. Based on previous findings, the YS and UTS for LPBF fabricated HIPed specimen was found to be 82MPa and 124MPa, respectively. The fatigue test was performed at two stress levels: one near the YS at 64MPa and the other at UTS at 124MPa. Three specimens followed the same orientation under each stress level. A sinusoidal waveform at 50Hz and R-value of 0.1 at room temperature of 22°C and 45% humidity was maintained throughout the fatigue test.

Hardness Test

Struers Duramin-A300 (Struers, Cleveland, OH, USA) hardness tester was used, followed by Vickers (HV) scale for the measurements. 100gf and a dwell time of 5 seconds were applied for the test. Three numbers of indentations with separated nominal spacings of 1mm were done on two vertical (X and Y) and horizontal (Z) samples. The average of the indentations was used to calculate the hardness. Satorius CP124S weight balance was used to determine the mass, and Accupyc II 1340 pycnometer was used to measure the volume by helium pycnometry. From these mass and volume measurements, density was calculated.

Microstructure characterization

For the characterization, the samples were derived from the unstressed portion of fatigue-tested specimens and cut into vertical and horizontal planes to analyze. Then ATM Opal 460 (Haan, Germany) mounting hot press was used to mount the cut samples in epoxy. Afterward, the samples were ground and polished with ATM SAPHIR 530 semi-automatic systems. After that, the samples were submerged for 10 seconds in Keller's etchant, and the microstructure was revealed using Olympus GX53 inverted optical microscope (Olympus Inc, Tokyo, Japan).

RESULTS AND DISCUSSION

Correlating Hardness value and Microstructure Characterization

The average density and hardness value of the specimens to printing orientation and aging hour is represented in Table 2. The density ranged from 2.65g/cm^3 to 2.66g/cm^3 for all test specimens, irrespective of the aging period. Hardness values measured from vickers micro indentation were consistent between horizontal and vertical planes, with lower HV values found for specimens aged 100h and 1000h. The microstructures of HIPed AlSi10Mg showed uniform distribution of Silicon (Si) particles in Figure 3. No visible microstructural changes can be concluded after observing aging time from 0 hours to 1000 hours. However, specimens aged for 1000h showed finer Si particles of size below 3µm.

Table 2: Density and hardness value based on printing orientation

Test Matrix HIPed AlSi10Mg	Thermally aged at 177°C							
	0 hours		10 hours		100 hours		1000 hours	
	XY	Z	XY	Z	XY	Z	XY	Z
Density *(g/cm^3)*	2.65	2.65	2.65	2.66	2.65	2.66	2.65	2.65
Hardness *(HV)*	60	59	59	60	49	60	45	47

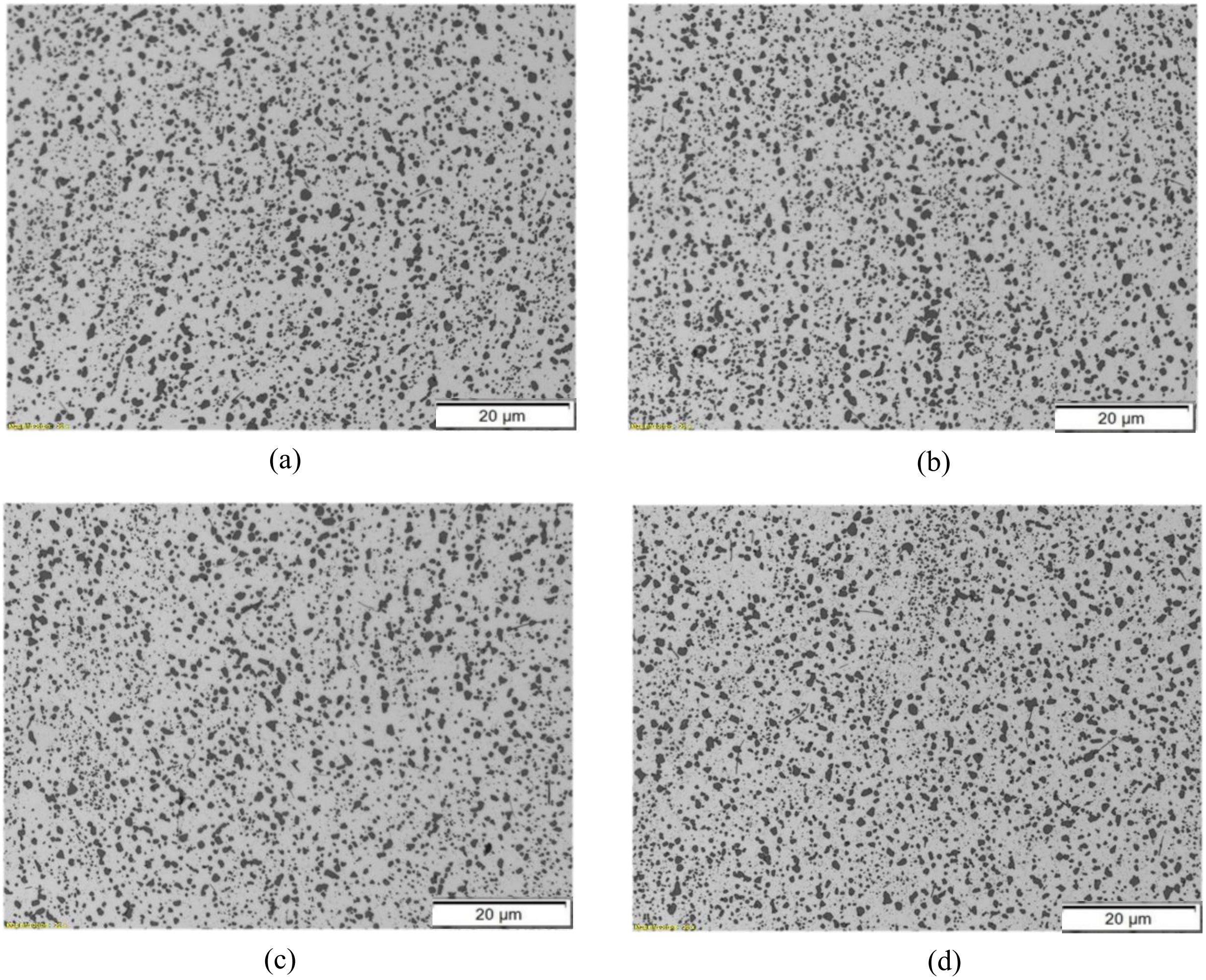

Figure 3: Microstructure of HIP AlSi10Mg showing uniformly displaying Si Particles. Aging time corresponds to a) 0, b)10, c)100 and d) 1000 hours at 177°C

Fatigue Properties

The evaluated fatigue properties for both: near YS at 62MPa and UTS at 124MPa for the aged HIP AlSi10Mg are represented in Table 3. The specimens tested at 75% (62MPa) of the YS, were able to surpass five million cycles and, therefore, discontinued. There was no visible crack or failure indicators observed for the specimens tested, as shown in Figure 4.

However, the fatigue specimens tested at UTS (124MPa) were prone to fracture at a different number of cycles in a visible correlation to their aging time, as shown in Table 3. The graph shown in Figure 5 presents the S-N plot for all the specimens tested at the UTS level (124MPa). The series of the graph consists of a group of three specimens each, and the names of the series indicate the HIP condition followed by aging time at 177°C (0h, 10h, 100h, and 1000h) and printing orientation (Z or XY). Progressive decay in the number of loading cycles was observed in Table 3 and Figure 5. The highest endurance was observed for the specimens that were not subjected to aging, and the lowest was found for the 1000h aged specimens: with a maximum 99% reduction in the number of cycles with respect to unaged specimens. An important observation concluded from this observation is that the average number of cycles of unaged XY and Z specimens dropped from 1.31 and 1.23 million cycles to 0.8 and 0.87 million cycles, respectively, which represents that even aging for 10h can reduce the number of load cycle by 29% to 38% with respect to their printing direction as shown in Table 3. The specimens aged for 100h fractured in a range between 0.49 million to 0.73 million cycles in Figure 5(a) and Figure 5(b). On the other hand, the endurance of the specimens aged for 1000h was observed to range from 0.01 million to 0.02 million load cycles. Surprisingly, one unaged Z specimen tested at UTS (124MPa) surpassed the threshold value of 5 million cycles and was discontinued (Table 3). This outlier specimen was not considered while calculating the average number of cycles in Table 3.

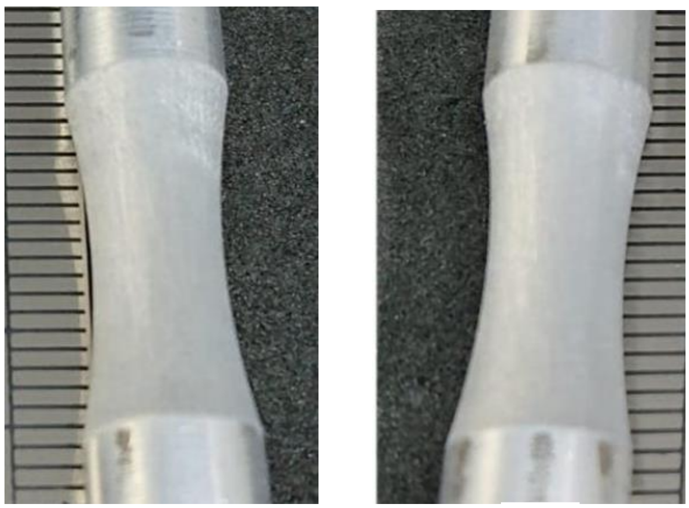

(a) (b)

Figure 4: Two Z- Specimens tested for fatigue after 5 million cycles at 62MPa: (a) Unaged, (b) 1000h Aged

Table 3: Evaluated fatigue properties Number of load cycles to failure (in Millions)

Test Matrix of AlSi10Mg HIPed Samples		Thermally aged at 177°C							
		0 hours		10 hours		100 hours		1000 hours	
		XY	Z	XY	Z	XY	Z	XY	Z
STRESS LEVEL	62MPa	+5	+5	+5	+5	+5	+5	+5	+5
	Average	+5	+5	+5	+5	+5	+5	+5	+5
	124MPa	1.22, 1.19, 1.53	1.21, 1.25, +5	0.77, 0.90, 0.75	0.72, 0.82, 1.06	0.73, 0.53, 0.49	0.63, 0.59, 0.68	0.02, 0.02, 0.02	0.01, 0.01, 0.02
	Average	1.31	1.23	0.81	0.87	0.58	0.63	0.02	0.01
Reduction in Number of Cycle (%)	Average	0	0	38%	29%	55%	48%	98%	99%

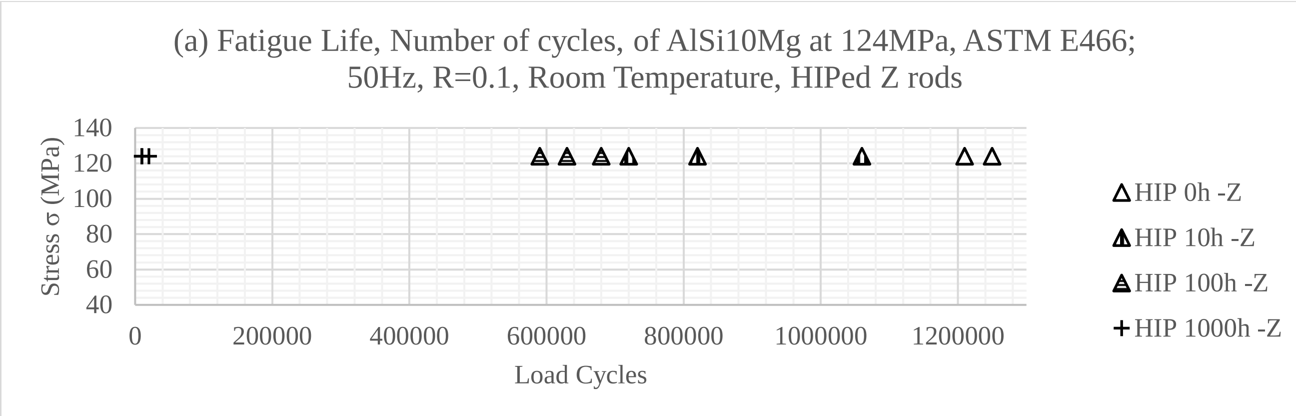

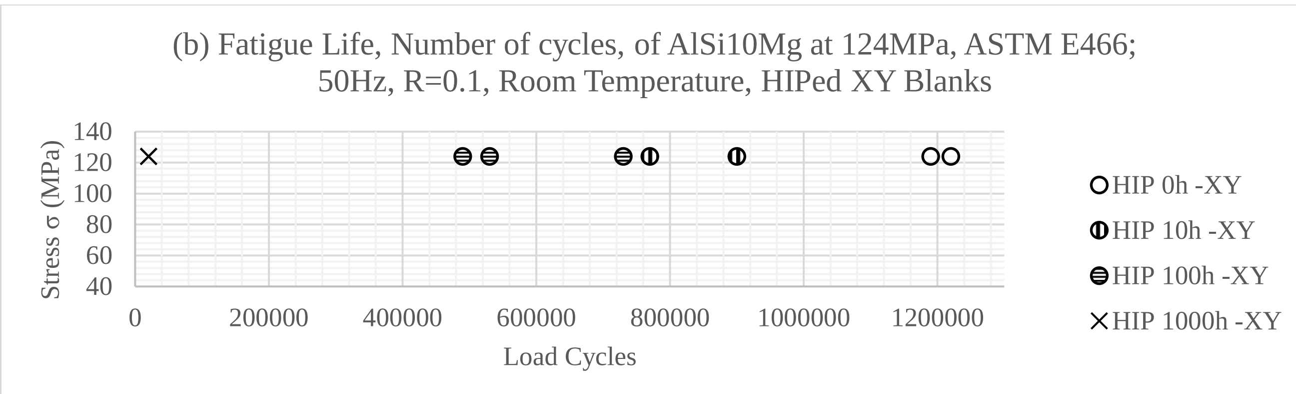

Figure 5: Number of load cycles at UTS 124MPa a) Z-Oriented Specimens, b) XY- Oriented Specimens

Investigation of the outlier specimen

From Table 3, one unaged specimen of Z orientation surpassed 5 million cycles and was investigated with respect to other Z-oriented specimens of the unaged group. The hardness values derived for these specimens were 55.6, 58.7, and 54.7, respectively (Table 4). Therefore, no solid conclusion to differentiate can be yielded from the hardness values. Figure 6 represents the microstructure of the unaged Z-oriented specimens. Here, also no notably visible difference was observed in microstructural features.

Table 4: Hardness Value of Z-oriented unaged Samples

Z- Orientation -0h aged	Hardness Value
1	55.6
2	58.7
3 (Outlier)	54.7

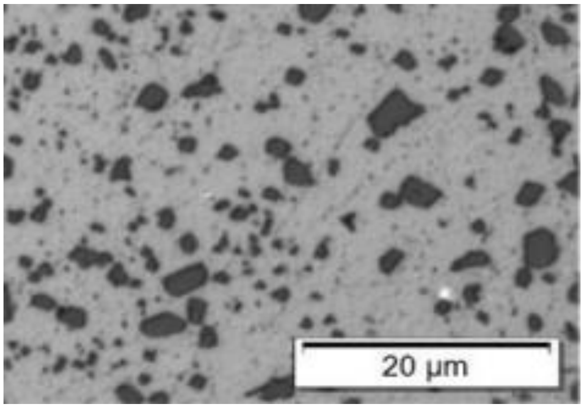

(a)

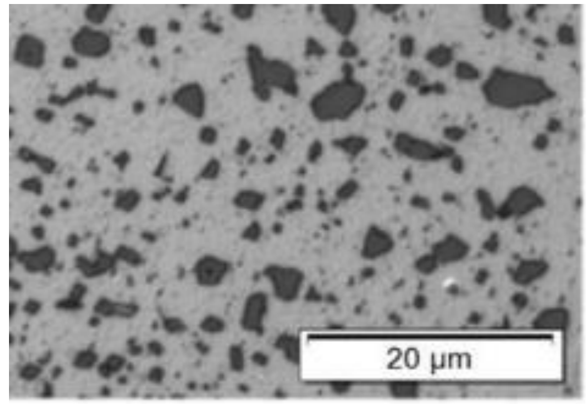

(b)

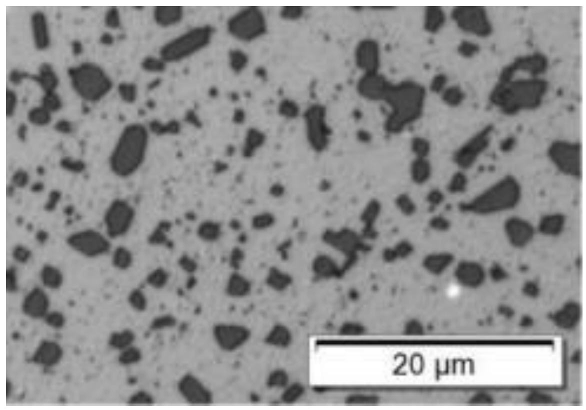

(c)

Figure 6: Microstructure of Z-oriented unaged Specimen (a) 1, (b) 2, (c) 3(outlier)

Failure Analysis

The fracture profiles shown in Figure 7 indicate that the specimens developed higher ductile features, such as reduced cross-section due to necking as well as cup and cone fracture modes with increased time of aging. The 1000h aged specimen demonstrated the highest ductility in fracture profile: showing well-defined cup and cone fracture features.

SEM fractography was further analyzed to observe the fracture surfaces of the Z and XY specimens at different aging times, as shown in Figure 8. It is observed that the fracture cross-section reduces with a longer aging time. Initially, it consists of a smooth texture with concentric lines merging to a crack initiation point and mapping out the directionality of crack propagation. Then, there is a rough surface which is the result of the rapid and final fracture. Higher aged specimens showed fewer features of these two textures due to ductility, which introduces more significant deformations accompanied by a more uniform stress distribution in the cross-section. Therefore, a higher uniform texture was observed for the longer thermally aged specimens in Figure 8.

In addition, smooth and rough textures corresponding to crack propagation on both 0h and 100h XY specimens were less rough in Z specimens. This suggests although it is commonly believed that HIP post-processing removes microstructural anisotropy caused in LPBF systems, It cannot be entirely eliminated. The rougher surfaces in Z-specimens than XY-specimens verify it.

High magnification SEM images were also examined where the rapid fracture occurred, as shown in Figure 9. It is seen that the fracture surface of the unaged Z specimen in Figure 9(a) had less voids and dimples in comparison to the surface of the Z specimen of 1000h aged in Figure 9(b). These differences were consistent and supported the previous observation on the fracture profiles and surfaces shown in Figure 7 and Figure 8, suggesting increased ductility for higher aged specimens.

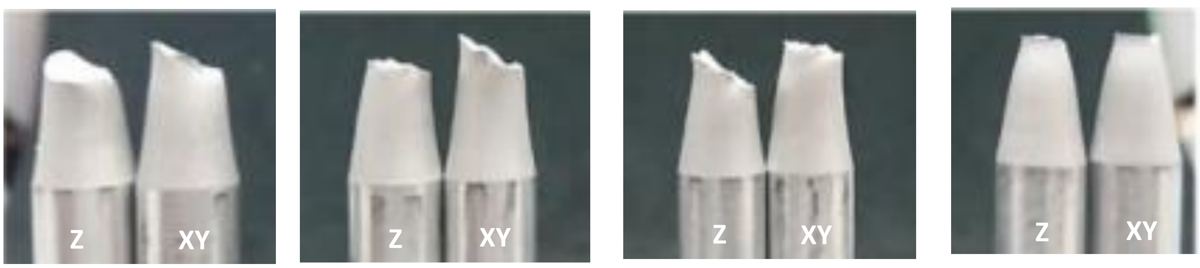

(a) (b) (c) (d)

Figure 7: Fracture profiles at different aging time (Z and XY) (a) 0h, (b)10h, (c)100h, (d) 1000h

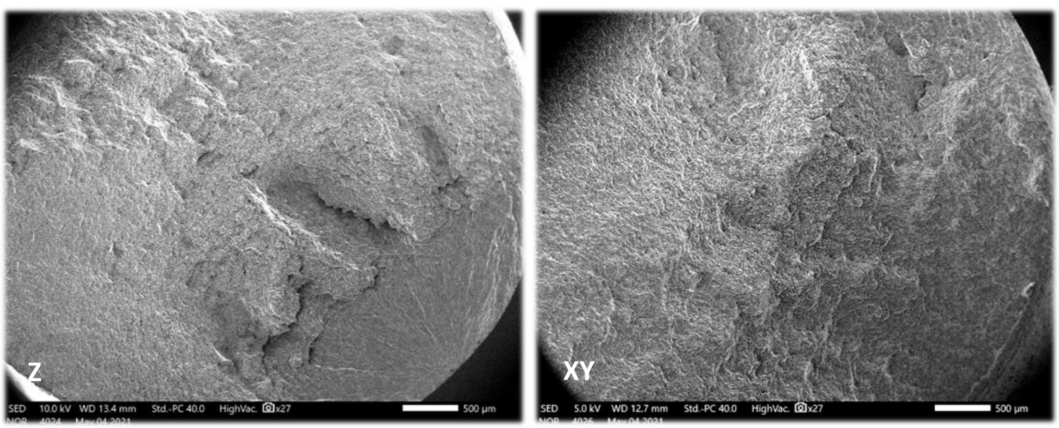

(a)

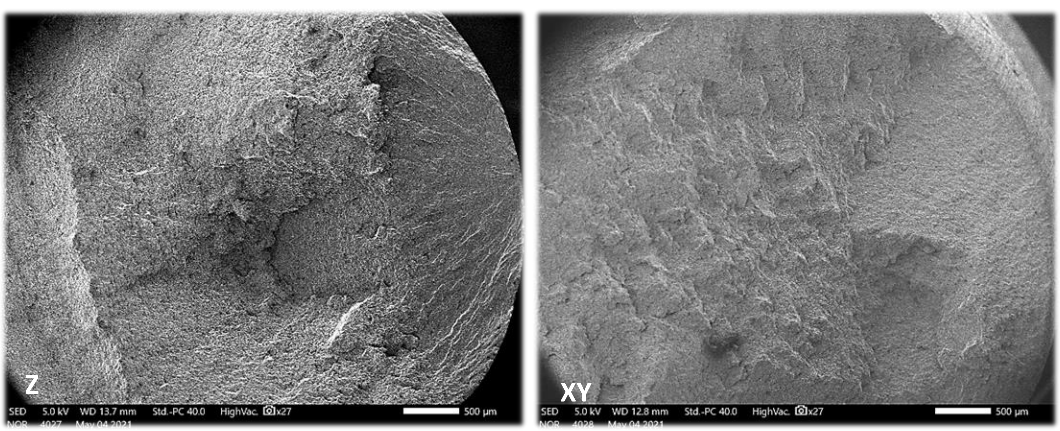

(b)

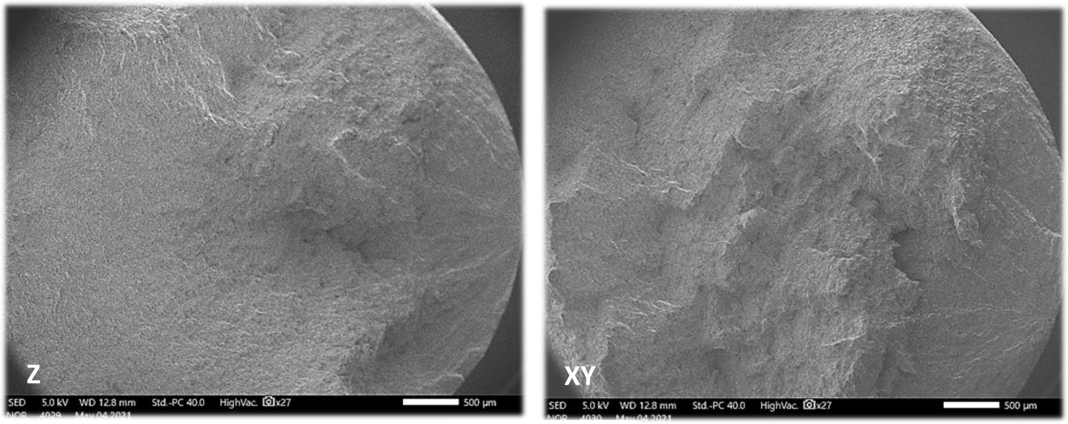

(c)

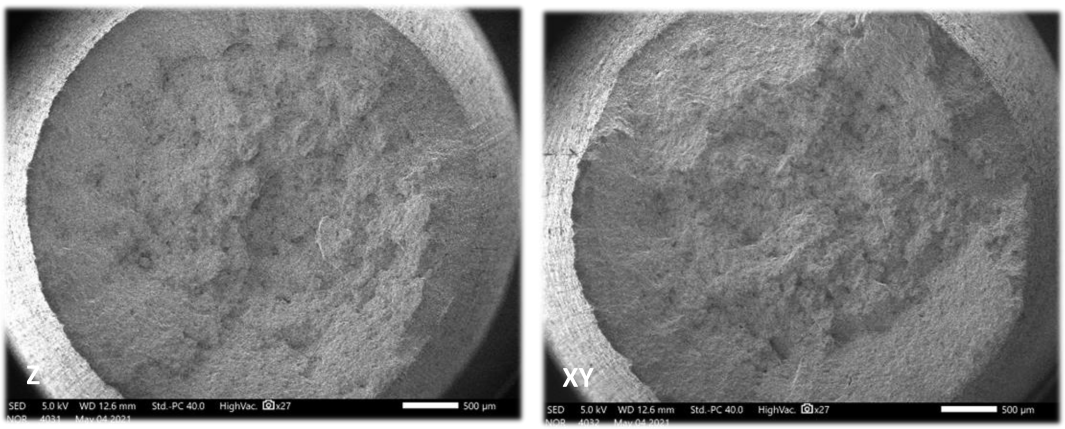

(d)

Figure 8: SEM fractography at different aging time (Z and XY) (a) 0h, (b)10h, (c)100h, (d) 1000h

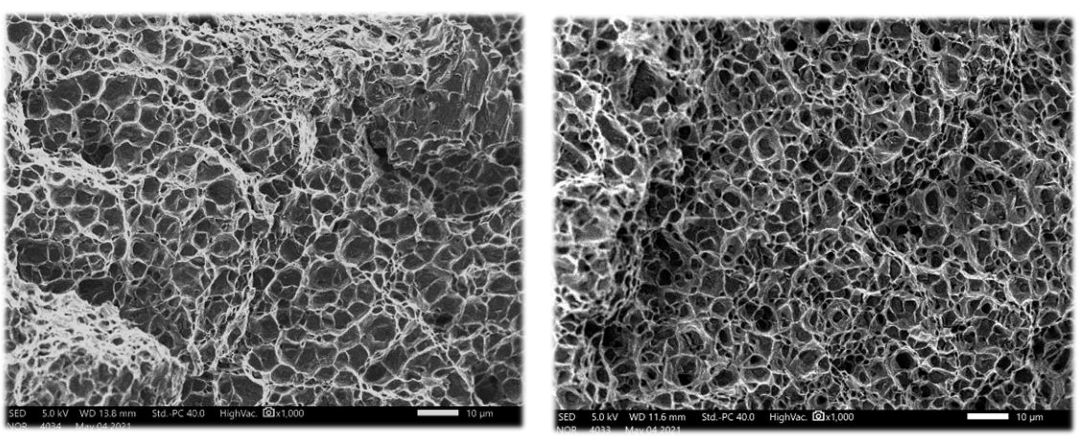

(a) (b)

Figure 9: High Magnification SEM fractography at different aging time Z- orientation (a) 0h, (b) 1000h

CONCLUSION

This research started with the goal of evaluating the fatigue performance of thermally aged L-PBF AlSi10Mg HIPed specimens. Therefore, L-PBF AlSi10Mg samples (built-in Z and XY directions) were HIPed and thermally aged for 0, 10h, 100h, and 100h at 177°C emulating the service condition. After that, the specimens went through a fatigue test: one near YS at 62MPa and another in UTS at 124MPa for evaluation.

Observing the microstructures, no evident change had been noticed at higher HIPed thermally aged samples. However, the fatigue test yielded dramatic results. For the fatigue test inspected near YS at 62MPa, the specimens in both directions lasted more than 5 million cycles and therefore discontinued.

On the other hand, specimens tested at UTS at 124MPa showed a dramatic reduction in the number of cycles with respect to aging time. It has been found that even 10 hours of thermal aging can reduce the fatigue life of a specimen by 29 to 30%, which is a considerable drop. Also, it was observed that 1000 hours of thermal aging reduce the fatigue life up to 98% of the fatigue life for the HIPed AlSi10Mg alloy fabricated from the LPBF machine.

Diving into the fracture surface from the UTS fatigue specimens, it was seen that prolonged thermal aging gradually promotes ductility. Features like reduced cross-section increased necking, and cup and cone fracture profiles are progressive toward the 1000 hours of aging, validating the increased ductility of specimens due to aging.

Furthermore, despite having identical fatigue endurance for both Z and XY specimens, the SEM fractography showed a noticeable difference between both. Z specimens had higher, less ductile textures in SEM fractography than the XY specimens. The ductility was less prominent for the 0h and 10h than the 100h and 1000h specimens. This suggests a future investigation of whether hot isostatic pressing can entirely eliminate the microstructural features of the inherent printing and to what degree of homogenization is allowed as ideal conditioning.

ACKNOWLEDGMENT

This research presented here was conducted at The University of Texas at El Paso within the W.M. Keck Center for 3D Innovation (Keck Center), a 13,000-sq. ft. state-of-the-art additive manufacturing facility. Additionally, equipment housed within the Department of Metallurgical, Materials, and Biomedical Engineering was utilized. Support for the research was provided, in part, by Mr. and Mrs. MacIntosh Murchison Chair I in Engineering with strategic investment in the development of this work by the UTEP Aerospace and Mechanical Engineering Department and the W.M. Keck Center for 3D Innovation.

REFERENCES

[1] E. M. Sefene, Y. M. Hailu, and A. A. Tsegaw, “Metal hybrid additive manufacturing: state-of-the-art,” *Progress in Additive Manufacturing*, 2022, doi: 10.1007/s40964-022-00262-1.

[2] J. E. Regis, A. Renteria, S. E. Hall, M. S. Hassan, C. Marquez, and Y. Lin, “Recent Trends and Innovation in Additive Manufacturing of Soft Functional Materials,” *Materials*, vol. 14, no. 16, p. 4521, Aug. 2021, doi: 10.3390/ma14164521.

[3] M. S. Hassan *et al.*, “Selective Laser Sintering of High-Temperature Thermoset Polymer,” *Journal of Composites Science*, vol. 6, no. 2, p. 41, Jan. 2022, doi: 10.3390/jcs6020041.

[4] Z. Duan *et al.*, “Pitting behavior of SLM 316L stainless steel exposed to chloride environments with different aggressiveness: Pitting mechanism induced by gas pores,” *Corrosion Science*, vol. 167, p. 108520, May 2020, doi: 10.1016/j.corsci.2020.108520.

[5] L. A. Chavez *et al.*, “Low-temperature selective laser sintering 3D printing of PEEK-Nylon blends: Impact of thermal post-processing on mechanical properties and thermal stability,” *Journal of Applied Polymer Science*, vol. 139, no. 23, p. 52290, Jun. 2022, doi: 10.1002/app.52290.

[6] L. E. Murr *et al.*, “Metal Fabrication by Additive Manufacturing Using Laser and Electron Beam Melting Technologies,” *Journal of Materials Science & Technology*, vol. 28, no. 1, pp. 1–14, Jan. 2012, doi: 10.1016/S1005-0302(12)60016-4.

[7] P. Gradl *et al.*, “Robust Metal Additive Manufacturing Process Selection and Development for Aerospace Components,” *Journal of Materials Engineering and Performance*, Apr. 2022, doi: 10.1007/s11665-022-06850-0.

[8] B. Barroqueiro, A. Andrade-Campos, R. A. F. Valente, and V. Neto, “Metal Additive Manufacturing Cycle in Aerospace Industry: A Comprehensive Review,” *Journal of Manufacturing and Materials Processing*, vol. 3, no. 3, p. 52, Jun. 2019, doi: 10.3390/jmmp30300s52.

[9] L. Yang *et al.*, *Additive manufacturing of metals: the technology, materials, design and production*. Springer, 2017.

[10] V. Mohanavel, K. S. Ashraff Ali, K. Ranganathan, J. Allen Jeffrey, M. M. Ravikumar, and S. Rajkumar, “The roles and applications of additive manufacturing in the aerospace and automobile sector,” *Materials Today: Proceedings*, vol. 47, pp. 405–409, 2021, doi: 10.1016/j.matpr.2021.04.596.

[11] B. O. Omiyale, T. O. Olugbade, T. E. Abioye, and P. K. Farayibi, “Wire arc additive manufacturing of aluminium alloys for aerospace and automotive applications: a review,” *Materials Science and Technology*, vol. 38, no. 7, pp. 391–408, May 2022, doi: 10.1080/02670836.2022.2045549.

[12] J. G. Kaufman and E. L. Rooy, *Aluminum alloy castings: properties, processes, and applications*. Asm International, 2004.

[13] V. S. Zolotorevsky, N. A. Belov, and M. v Glazoff, *Casting aluminum alloys*, vol. 12. Elsevier Amsterdam, 2007.

[14] Jorge. Merino *et al.*, "Multiple, comparative heat treatment and aging schedules for controlling the microstructures and mechanical properties of laser powder bed fusion fabricated AlSi10Mg alloy," *Journal of Materials Research and Technology*, vol. 13, pp. 669–685, Jul. 2021, doi: 10.1016/j.jmrt.2021.04.062.

[15] S. Sahoo, "Prediction of residual stress and deformation of build part with variation of hatch spacing in direct metal laser sintering of AlSi10Mg built part: Thermo-mechanical modeling," *Journal of Laser Applications*, vol. 33, no. 3, p. 032011, Aug. 2021, doi: 10.2351/7.0000393.

[16] U. Patakham, A. Palasay, P. Wila, and R. Tongsri, "MPB characteristics and Si morphologies on mechanical properties and fracture behavior of SLM AlSi10Mg," *Materials Science and Engineering: A*, vol. 821, p. 141602, Jul. 2021, doi: 10.1016/j.msea.2021.141602.

[17] C. C. Roth, T. Tancogne-Dejean, and D. Mohr, "Plasticity and fracture of cast and SLM AlSi10Mg: High- testing and modeling," *Additive Manufacturing*, vol. 43, p. 101998, Jul. 2021, doi: 10.1016/j.addma.2021.101998.

[18] A. Kempf and K. Hilgenberg, "Influence of heat treatments on AlSi10Mg specimens manufactured with different laser powder bed fusion machines," *Materials Science and Engineering: A*, vol. 818, p. 141371, Jun. 2021, doi: 10.1016/j.msea.2021.141371.

[19] J. C. Hastie, J. Koelblin, M. E. Kartal, M. M. Attallah, and R. Martinez, "Evolution of internal pores within AlSi10Mg manufactured by laser powder bed fusion under tension: As-built and heat treated conditions," *Materials & Design*, vol. 204, p. 109645, Jun. 2021, doi: 10.1016/j.matdes.2021.109645.

[20] J. H. Rao, P. Rometsch, X. Wu, and C. H. J. Davies, "The processing and heat treatment of selective laser melted Al-7Si-0.6Mg alloy," *Additive Manufacturing for the Aerospace Industry*, pp. 143–161, Jan. 2019, doi: 10.1016/B978-0-12-814062-8.00008-X.

[21] F. Trevisan *et al.*, "On the Selective Laser Melting (SLM) of the AlSi10Mg Alloy: Process, Microstructure, and Mechanical Properties," *Materials*, vol. 10, no. 1, p. 76, Jan. 2017, doi: 10.3390/ma10010076.

[22] M. Tocci, A. Pola, M. Gelfi, and G. M. la Vecchia, "Effect of a New High-Pressure Heat Treatment on Additively Manufactured AlSi10Mg Alloy," *Metallurgical and Materials Transactions A*, vol. 51, no. 9, pp. 4799–4811, Sep. 2020, doi: 10.1007/s11661-020-05905-y.

[23] Longchao. Zhuo *et al.*, "Effect of post-process heat treatment on microstructure and properties of selective laser melted AlSi10Mg alloy," *Materials Letters*, vol. 234, pp. 196–200, Jan. 2019, doi: 10.1016/j.matlet.2018.09.109.

[24] N. T. Aboulkhair, I. Maskery, C. Tuck, I. Ashcroft, and N. M. Everitt, "The microstructure and mechanical properties of selectively laser melted AlSi10Mg: The effect of a conventional T6-like heat treatment," *Materials Science and Engineering: A*, vol. 667, pp. 139–146, Jun. 2016, doi: 10.1016/j.msea.2016.04.092.

[25] F. Alghamdi, X. Song, A. Hadadzadeh, B. Shalchi-Amirkhiz, M. Mohammadi, and M. Haghshenas, "Post heat treatment of additive manufactured AlSi10Mg: On silicon morphology, texture and small-scale properties," *Materials Science and Engineering: A*, vol. 783, p. 139296, May 2020, doi: 10.1016/j.msea.2020.139296.

[26] X. Jiang, W. Xiong, L. Wang, M. Guo, and Z. Ding, "Heat treatment effects on microstructure-residual stress for selective laser melting AlSi10Mg," *Materials Science and Technology*, vol. 36, no. 2, pp. 168–180, Jan. 2020, doi: 10.1080/02670836.2019.1685770.

[27] O. Ertuğrul *et al.*, "Effect of HIP process and subsequent heat treatment on microstructure and mechanical properties of direct metal laser sintered AlSi10Mg alloy," *Rapid Prototyping Journal*, vol. 26, no. 8, pp. 1421–1434, Jun. 2020, doi: 10.1108/RPJ-07-2019-0180.

[28] N. Read, W. Wang, K. Essa, and M. M. Attallah, "Selective laser melting of AlSi10Mg alloy: Process optimisation and mechanical properties development," *Materials & Design (1980-2015)*, vol. 65, pp. 417–424, Jan. 2015, doi: 10.1016/j.matdes.2014.09.044.

[29] V. J. Matjeke, C. Moopanar, A. S. Bolokang, and J. W. van der Merwe, "Effect of heat treatment time on the microstructure and mechanical deformation behavior of additive-manufactured AlSi10Mg components," *Progress in Additive Manufacturing*, vol. 5, no. 4, pp. 379–385, Dec. 2020, doi: 10.1007/s40964-020-00139-1.

[30] N. T. Aboulkhair, M. Simonelli, L. Parry, I. Ashcroft, C. Tuck, and R. Hague, "3D printing of Aluminium alloys: Additive Manufacturing of Aluminium alloys using selective laser melting," *Progress in Materials Science*, vol. 106, p. 100578, Dec. 2019, doi: 10.1016/j.pmatsci.2019.100578.

[31] W. Li *et al.*, "Effect of heat treatment on AlSi10Mg alloy fabricated by selective laser melting: Microstructure evolution, mechanical properties and fracture mechanism," *Materials Science and Engineering: A*, vol. 663, pp. 116–125, Apr. 2016, doi: 10.1016/j.msea.2016.03.088.

[32] "Technical Data EOS M290 ," *EOS*. https://www.eos.info/en/additive-manufacturing/3d-printing-metal/eos-metal-systems/eos-m-290 (accessed Jun. 05, 2022).

[33] "EOS Aluminium AlSi10Mg Material Data Sheet Metal Solutions." Accessed: Jun. 05, 2022. [Online]. Available: https://www.eos.info/03_system-related-assets/material-related-

contents/metal-materials-and-examples/metal-material-datasheet/aluminium/material_datasheet_eos_aluminium-alsi10mg_en_web.pdf

[34] "ASTM International, ASTM F3318-18, Standard for Additive Manufacturing – Finished Part Properties – Specification for AlSi10Mg with Powder Bed Fusion – Laser Beam, I," p. 7, 2018, doi: 10.1520/F3318-18.

[35] "ASTM International, ASTM E466-15, Standard Practice for Conducting Force Controlled Constant Amplitude Axial Fatigue Tests of Metallic Materials," *ASTM International*, p. 6, 2015, doi: 10.1520/E0466-15.